CHEMISTRY OF MATERIALS

pubs.acs.org/cm

Article

Cooperativity and Metal−Linker Dynamics in Spin Crossover Framework Fe(1,2,3-triazolate)$_2$

Anastasia B. Andreeva, Khoa N. Le, Kentaro Kadota, Satoshi Horike, Christopher H. Hendon,* and Carl K. Brozek*

Cite This: https://doi.org/10.1021/acs.chemmater.1c03143

Read Online

ACCESS | Metrics & More | Article Recommendations | Supporting Information

ABSTRACT: Cooperative interactions are responsible for the useful properties of spin crossover (SCO) materials—large hysteresis windows, critical temperatures near room temperature, and abrupt transitions—with hybrid framework materials exhibiting the greatest cooperativity and hysteresis of all SCO systems. However, little is known about the chemical origin of cooperativity in frameworks. Here, we present a combined experimental−computational approach for identifying the origin of cooperativity in the metal−organic framework (MOF) Fe(1,2,3-triazolate)$_2$ (Fe(TA)$_2$), which exhibits the largest known hysteresis window of all SCO materials and unusually high transition temperatures, as a roadmap for understanding the manipulation of SCO behavior in general. Variable-temperature vibrational spectroscopy provides evidence that "soft modes" associated with dynamic metal−linker bonding trigger the cooperative SCO transition. Thermodynamic analysis also confirms a cooperativity magnitude much larger than those of other SCO systems, while electron density calculations of Fe(TA)$_2$ support previous theoretical predictions that large cooperativity arises in materials where SCO produces considerable differences in metal−ligand bond polarities between different spin states. Taken together, this combined experimental−computational study provides a microscopic basis for understanding cooperative magnetism and highlights the important role of dynamic bonding in the functional behavior of framework materials.

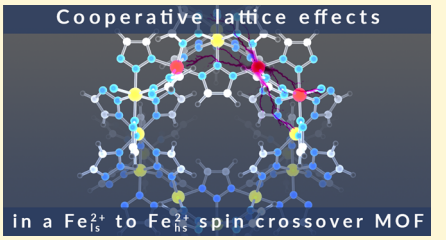

INTRODUCTION

Switchable behavior in materials is often designed to be abrupt and reversible, have large "memory" (hysteresis), and are triggerable by stimuli near ambient conditions. Spin crossover (SCO) is a leading example of switchable magnetism that arises from paramagnetic systems in equilibrium between high-spin (HS) and low-spin (LS) electronic configurations.[1−4] With stimuli such as thermal energy, light, guest adsorption, or pressure, the equilibria can be reversibly shifted to the magnetic state by influencing the bonding environment of the magnetic center. Relatively low-energy input is required to convert between the spin states in SCO systems because the spin-pairing destabilization energy of the LS state equals the crystal-field destabilization energy of the HS state. As octahedral Fe^{2+} comprises the great majority of SCO systems, it serves as the standard model for explicating key concepts, as follows. Low temperature favors the LS state because $t_{2g}^6e_g^0$ electronic configurations have less metal−ligand antibonding character and hence greater enthalpic stability compared to the $t_{2g}^4e_g^2$ HS states, while moderate temperatures, often below 300 K, favor the HS state due to its greater vibrational entropy.[5,6] Due to the impact of SCO on the electronic properties of the magnetic ions, spectroscopy can be used in addition to magnetic measurements to monitor the SCO process, including electronic absorption and ^{57}Fe Mössbauer spectroscopy.[7] Although molecular SCO complexes typically exhibit gradual spin transitions at temperatures below 300 K without magnetic hysteresis, solid-state SCO systems display abrupt transitions with magnetic hysteresis near room temperature, rendering them more useful for readable "on-off" technology.[8] Nearly all solid-state examples are porous frameworks such as the Prussian Blue analogues or the Hofmann-type networks (Fe(L)M(CN)$_4$, L = pyrazine or pyridine, M = Co, Ni, Pd, Pt),[9−18] with Fe(py)$_2$Ni(CN)$_4$ as the seminal example,[11] while the largest SCO hysteresis has been observed in the metal−organic framework (MOF) Fe(1,2,3-triazolate)$_2$ (Fe(TA)$_2$), as shown in Figure 1.[19] Despite the importance of abrupt and hysteretic spin transitions, the specific chemistry responsible for these long-range phenomena is just beginning to emerge.

Several models[20−23] describe "cooperative interactions" as the origin of solid-state SCO behavior and successfully reproduce SCO phenomena, but they generally lack insight into the chemical meaning of such interactions. Despite its ambiguity, cooperativity is a measurable thermodynamic quantity. For example, fitting spin transition equilibrium data of solid systems to a noninteracting model[24] meant for

Received: September 10, 2021
Revised: October 12, 2021

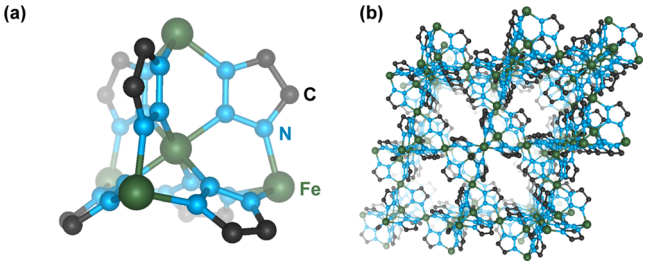

Figure 1. Representation of the $Fe(TA)_2$ metal node (a) and pore structure (b).

molecular SCO systems grossly overestimates ΔH and ΔS of the spin transition compared to values measured from differential scanning calorimetry. A cooperative interaction parameter Γ is thus employed to account for the apparent thermodynamic stabilization of solid-state systems.[25] Theoretical descriptions of SCO associate Γ with vibronic interactions and coupled anharmonic oscillations between neighboring magnetic centers.[21,26,27] Although the dominant effect of Γ is to lower ΔH, the large vibrational ΔS of spin transitions has also been identified as a possible contributor to cooperativity.[21] Based on our previous work on dynamic metal−linker bonding in MOFs,[28] we hypothesized that vibrational "soft modes" drive the large cooperativity of SCO frameworks, just as they trigger other types of phase changes through coupled lattice dynamics. Specifically, we propose that certain vibrations act as "soft modes" by driving metal−ligand bonds to convert between strong and weak interactions, thereby enabling the huge volumetric expansion from the condensed LS state into the HS form, as shown in Scheme 1a. Recently, we reported

Scheme 1. Representation of Bonding and Hysteresis Phenomena in Spin Crossover Behavior[a]

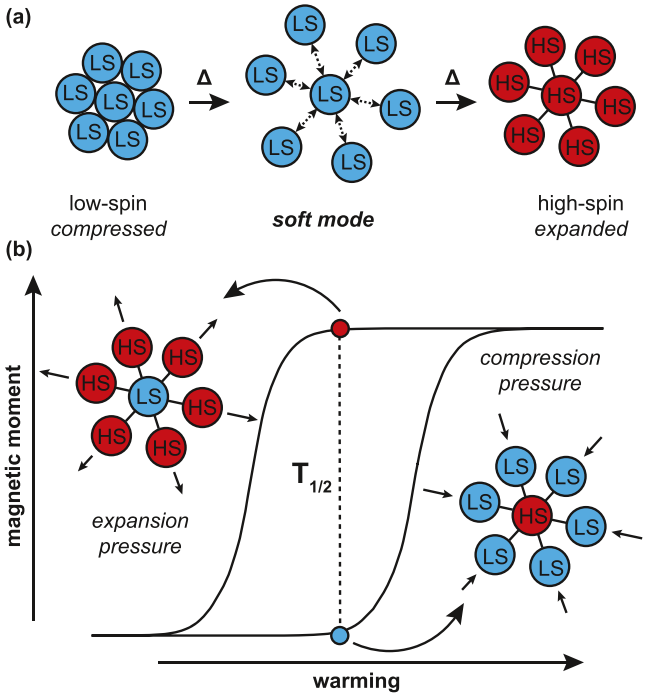

[a](a) Thermal-induced bond expansion and soft modes. (b) Magnetic hysteresis and abrupt transitions with depictions of elastic interactions between neighboring ions.

that the strong temperature dependence of MOF optical absorption arises in part from this thermally activated dynamic bonding.[29] Furthermore, we propose that this dynamic bonding also serves as the mechanism of both large hysteresis and abrupt transitions of SCO frameworks: the large hysteresis arises from the "expansion pressure" of neighboring HS centers forcing minority LS centers back into the HS state and the vice versa scenario for "compression pressure", causing SCO to occur at lower and higher temperatures, respectively, compared to the expected $T_{1/2}$ for a system without cooperative interactions (Scheme 1b). Dynamic bonding would therefore assist in the reversible bond configurations and coupled motion of neighboring atoms in this mechanism, while also causing the abrupt transitions because as lattice phonons, they drive the collective motion of the entire lattice simultaneously.

Here, we report a combined experimental−computational investigation into the origin of the exceptional SCO cooperativity of $Fe(TA)_2$. Variable-temperature diffuse reflectance infrared vibrational spectroscopy (VT-DRIFTS) provides evidence for dynamic metal−linker bonding in the family of isostructural $M(TA)_2$ materials (M = Mn, Fe, Co, Cu, Zn) reminiscent of the "loose−tight" equilibrium phase change observed for conventional carboxylate MOFs.[28] In addition to dynamic bonding, the vibrational spectra of $Fe(TA)_2$ depict hallmark signatures of soft modes at the SCO critical temperature, suggesting a microscopic origin of cooperativity. Thermodynamic analysis of the SCO equilibrium also allows cooperativity to be quantified, revealing an unusually large magnitude that explains the wide magnetic hysteresis. Finally, computational analysis suggests that this large cooperativity arises from the ionic and polarizable bonding inherent to MOF materials and other systems with metal ions bridged by azolates and similar ligands. Compared to other classes of SCO molecules and materials, these results explain why ionically bound networks of metal−organic bridges are uniquely well-suited building blocks for switchable magnetism, while raising fundamental questions concerning the general importance of dynamic bonding in the phase-change behavior of porous materials.

METHODS

Materials. All commercial chemicals were used as received unless stated otherwise. Copper(II) hydroxide (technical grade, Aldrich), 1*H*-1,2,3-triazole (>98%, TCI), *N*,*N*-dimethylformamide (DMF, ACS grade, Fisher Scientific), ammonium hydroxide (30% NH_4OH, ACS grade, Baker), ethanol (EtOH, 100%, Decon), iron(II) chloride (98%, anhydrous, Strem), manganese(II) nitrate tetrahydrate solution (98%, Alfa Aesar), zinc(II) chloride (>98%, reagent grade, Sigma-Aldrich), anhydrous cobalt(II) chloride (97%, anhydrous, Alfa Aesar), and methanol (MeOH, HPLC grade, Oakwood Chemical). Solvothermal syntheses were conducted in 20 mL scintillation vials charged with stir bars heated in an aluminum dry bath or in a Yamato Convection oven unless stated otherwise.

Characterization. Variable-temperature diffuse reflectance infrared Fourier transform (VT-DRIFT) spectra were recorded on a Nicolet 6700 FT-IR spectrometer equipped with a Transmission E.S.P. attachment and a MCT-A detector paired with a Harrick Scientific Praying Mantis Diffuse Reflection (DRP) accessory. Introduction of vacuum and temperature variation was possible with a Harrick Scientific low-temperature reaction chamber (CHC) equipped with UV quartz and 2 Harrick 15 mm × 2 mm potassium bromide windows. To maximize the intensity, all samples were diluted with potassium bromide. Reflectance FT-IR spectra were obtained in the range of 4000−650 cm^{-1} with 0.9820 cm^{-1} resolution and 32 scans. Variable-temperature powder X-ray diffraction (PXRD)

https://doi.org/10.1021/acs.chemmater.1c03143
Chem. Mater. XXXX, XXX, XXX−XXX

Table 1. Thermodynamic Properties of Spin Crossover Frameworks and Molecules[a*,b]

	ΔH (kJ mol^{-1})		ΔS (J K^{-1} mol^{-1})		$T_{1/2}$ (K)			
name	heating	cooling	heating	cooling	heating	cooling	hysteresis window (K)	ref
$Fe(TA)_2$	31.2	33.3	53.6	71.6	582	465	117	
$Fe(trz)(Htrz)_2BF_4$	25.5	26.7	66.6	77.8	383	343	40	35
$Fe(py)_2Ni(CN)_4$	14.9*		74.2*		209	191	18	36
$Fe(py)_2Pt(CN)_4$	13.7	13.1	65.2	70.3	242	221	21	37
$Fe(pz)Pt(CN)_4$		21*		81*	302	286	16	38
$Fe(pz)Ni(CN)_4$	14.5*		51*		295	279	26	38
$Fe((bpac)Au(CN)_2)_2$	15	14	67	64	228	220	5	39
$Fe(ptz)_6(BF_4)_2$		6.1		61.2		100		24
$PhB(MesIm)_3Fe(NPPh_3)$		14.2		175.9		81		40
$Fe(phen)_2(NCS)_2$	8.6		48.8		176			26
$Fe(PM\text{-}AzA)_2(NCS)_2$	6.7		35.3		189			41

[a*]Calculated average from endothermic and exothermic peaks. [b]Trz = 1,2,4-triazolato; py = pyridine; pz = pyrazine; bpac = 1,2-bis(4′-pyridyl)acetylene; ptz = 1-propyltetrazole; $PhB(MesIm)_3Fe{-}N{=}PPh_3$ = iron(II) phosphoraniminato; phen = 1,10-phenanthroline; PM-AzA = *N*-2′-pyridylmethylene-4-(phenylazo)aniline.

patterns were collected under a N_2 stream using a BTS 500 high-temperature attachment on a Rigaku MiniFlex with a Cu Kα anode (λ = 1.5418 Å). Air-sensitive [$Fe(TA)_2$] was packed in the attachment inside an Ar-filled glove box. The PXRD patterns were indexed, and the obtained cell parameters were refined by the Le Bail method using EXPO2014.[30] Linear coefficients of thermal expansion (CTE) were calculated from the cell lengths and temperatures as summarized in Table S1. Differential scanning calorimetry (DSC) was performed on a TA Instruments Differential Scanning Calorimeter (DSC Q2500).

Equilibrium Model and Fitting Parameters. The equilibrium model explores whether the metal−nitrogen red shifts arise from temperature-dependent intensities of two overlapping bands. Supposing an equilibrium is present as A ⇌ B with K_{eq} = [B]/[A], we assume A to be a "tight" M−N state with vibrational energy ν_A, and B to be a "loose" state with vibrational energy ν_B, where $\nu_A > \nu_B$. Rather than describing two specific metal−nitrogen configurations, the two states represent ensembles of configurations in shallow potential energy surfaces that appear more tight or loose. Therefore, the equilibrium will shift to the "loose" state at higher temperatures. Since $\nu_A > \nu_B$, statistically, a red shift should be observed. Using x_A and x_B to denote the mole fraction of A and B, $x_A = 1/(1 + K_{eq})$ and $x_B = K_{eq}/(1 + K_{eq})$. Similarly, we define the apparent peak position to be $x_A\nu_A + x_B\nu_B$ at T, and $x_{A'}\nu_A + x_{B'}\nu_B$ at T'. After substituting $K_{eq} = \exp[-\Delta G^\circ/(RT)]$, we get an expression for the red shift as a function of temperature that is fundamentally equivalent to the Boltzmann expressions in the Morse and cross-anharmonicity models. Using a global fitting procedure, we extract ν_A and ν_B from our experimental data and assume that all the peaks at each temperature can be deconvoluted into the sum of two Gaussian peaks A and B with fixed frequencies but variable areas and peak widths. Using this method for $Fe(TA)_2$, we find ν_A = 1228.6 cm^{-1} and ν_B = 1224.1 cm^{-1}. We define the equilibrium constant by the ratio of the areas $K = Area_B/Area_A$ and plot K as a function of T. Conventionally, ln K would be plotted as a function of $1/T$ for van't Hoff analysis. However, noticing the deviation from a straight line in the van't Hoff plot, we attributed this deviation to a contribution from the nonzero heat capacity change in this process, which resulted in modification from $K = \exp[-(\Delta H - T\Delta S)/(RT)]$ to $K = \exp[-(\Delta H_R + \Delta C_P(T - T_R) - T(\Delta S_R + \Delta C_P \ln(T/T_R)))/(RT)]$, with the reference temperature T_R set to 298.15 K. The second fitting results in ΔH_R = 14.5 kJ mol^{-1}, ΔS_R = 39.6 J mol^{-1} K^{-1}, and ΔC_P = 119.7 J mol^{-1} K^{-1}.

Computational Methods. Structural relaxation for all structures was performed with DFT calculations as implemented in the Vienna Ab initio Simulation Package (VASP, version 5.4.4).[31] All calculations were performed with a plane-wave cut off at 500 eV and the unrestricted GGA-PBEsol exchange−correlation functional.[32] The ionic convergence criterion was set to 0.005 eV Å^{-1} and the electronic convergence criterion was set to 10^{-6} eV. The automatic k-grid used for all optimizations was 3 × 3 × 3. Symmetry was not enforced for these calculations. The optimized room temperature (RT) structures of the Zn, Co, and Mn analogues were obtained by spin-polarized calculations. The high-temperature structures were obtained by expanding the cells and then optimized by spin-polarized calculations with restricted changes in the cell volume and shape. The Fe analogues were obtained by similar methods as above, but for the RT structure, the spin moments on all Fe atoms were set to 0, and for the HT structures, the spin moment for each Fe atom was set to 4. Similarly, for the Cu analogue, the spin moment for RT and HT were set to match the experimentally reported data.[33] Energy profiles for all structures were obtained by a similar technique where the unit cell is compressed and expanded from optimized ground-state structures and then reoptimized with restricted change in the cell shape and volume.

Vibrational frequency calculations were obtained via the finite difference method (FDM) as implemented in VASP where zone-center (Γ-point) frequencies were calculated. The calculations were carried out with the unrestricted GGA-PBEsol exchange−correlation functional and with similar convergence criteria as relaxation calculations. Electronic properties for all systems were obtained from single-point calculations at the Γ-point with the HSEsol06 functional.[34]

RESULTS AND DISCUSSION

Table 1 summarizes the key thermodynamic parameters for a representative collection of SCO molecules and frameworks. Entries 1−7 are solid-state networks and 8−11 are molecules. The critical temperature ($T_{1/2}$) at which HS and LS populations become equal (50:50) clearly distinguishes between each class of the SCO system, with molecules exhibiting the lowest temperatures and MOFs the highest. This temperature is governed by $\Delta H/\Delta S$ because ΔG = 0 at this condition, such that the differences between the $T_{1/2}$ values mostly arise from differences in ΔH. Solid-state systems (entries 1−7) also display a hysteresis with two critical temperatures ($T_{heating}$ and $T_{cooling}$). Both the hysteresis and higher $T_{1/2}$ values have been attributed to cooperative interactions present in covalent and ionic solids that are largely absent in molecular crystals since they feature only weak intermolecular forces between isolated molecules. Although Prussian Blue and Hofmann-type frameworks resemble MOFs, $T_{heating}$ and $T_{cooling}$ of $Fe(TA)_2$ are approximately twice as high with a ten-times wider hysteresis window.

To identify the origin of the unexpected SCO behavior of $Fe(TA)_2$ and its relation to cooperativity, we investigated the

https://doi.org/10.1021/acs.chemmater.1c03143
Chem. Mater. XXXX, XXX, XXX−XXX

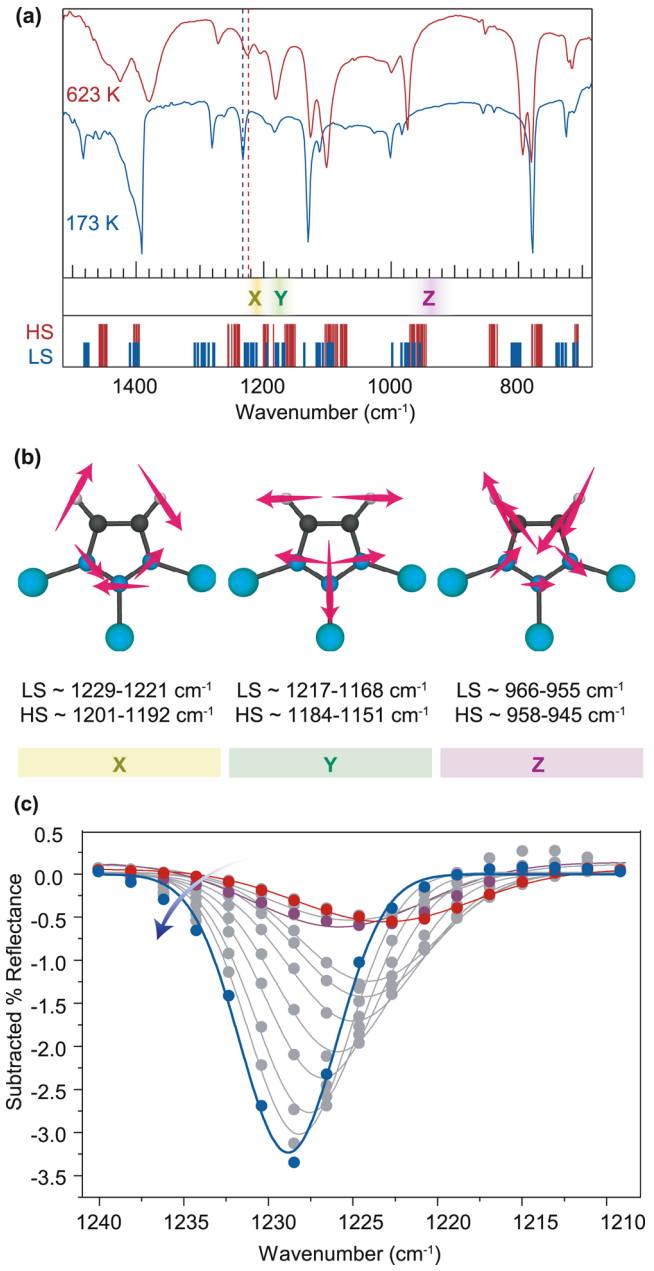

Figure 2. VT-DRIFT spectra of $Fe(TA)_2$. (a) Spectra collected at 623 and 173 K of HS and LS phases, respectively. (b) Computed vibrational modes corresponding to frequency regions X, Y, and Z. (c) Baseline-subtracted VT spectra of mode X fitted to a Gaussian function.

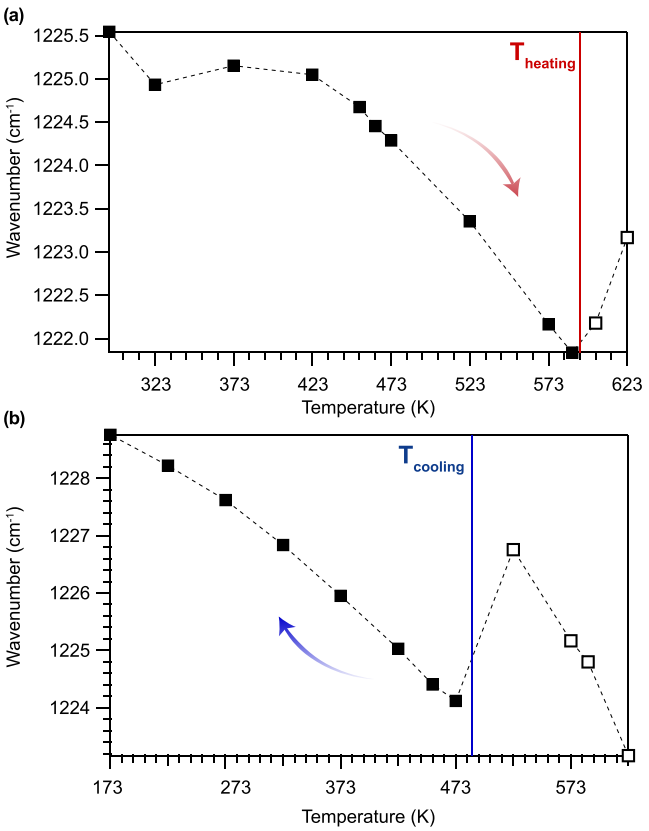

Figure 3. Peak maxima of vibrational mode "X" versus temperature. (a) Peak maxima collected during heating. (b) Peak maxima collected during cooling. Filled data correspond to $Fe(TA)_2$ in the LS state and hollow to the HS state, respectively.

dynamic bonding of $M(TA)_2$ frameworks. Bulk powder XRD of $Fe(TA)_2$ was obtained by the original Yaghi et al. method. Briefly, $FeCl_2$ was combined with 1,2,3-triazole in DMF under air-free conditions and heated to 120 °C affording a pink solid, with PXRD analysis confirming the phase purity (Figure S22). The related isostructural frameworks with Mn, Co, and Zn were also prepared according to the original report by Yaghi et al.[42] while the Cu material was prepared by the Volkmer procedure.[33] To explore whether $M(TA)_2$ frameworks engage in the same "loose−tight" dynamic bonding equilibrium as carboxylate MOFs, VT-DRIFT spectra were recorded between 173 and 623 K under dynamic vacuum. In Figure 2a the 173 K (LS) and 623 K (HS) spectra of $Fe(TA)_2$ are plotted with computed vibrational transitions of both HS and LS materials (Figure 2b), showing a good overall agreement. As expected for two different phases, the LS and HS spectra show considerable differences, with several bands disappearing and new bands appearing with decreased temperature (Figure 2a). This effect is also apparent in the different expected bands from the calculated phonon modes. Figure 2a,b highlights vibrations labeled X, Y, and Z that persist with temperature, which, as calculations suggest, involve triazolate-based stretches. Interestingly, vibration X, centered at around 1230 cm^{-1}, displays temperature dependence whereas Y and Z do not. Figure 2c plots the baseline-subtracted spectra of vibration X for $Fe(TA)_2$ during a cooling cycle. Although carboxylate MOFs exhibit carboxylate stretches that red-shift linearly at higher temperatures, close inspection indicates that this triazolate mode exhibits both red- and blue-shifts with temperature.

Figure 3a plots the peak maxima of vibration X in $Fe(TA)_2$ during a heating cycle, revealing a red-shift−blue-shift inflection centered at $T_{heating}$, while Figure 3b shows a similar trend centered at $T_{cooling}$ during a cooling cycle. A red-shift−blue-shift inflection is hallmark evidence of the special class of vibrations known as soft modes that trigger phase transitions by pushing the atomic positions from one phase to the positions of another. As the material approaches the T_c of a phase transition, soft modes impart increasing amounts of energy to the surrounding lattice through coupled anharmonic oscillations. As a result, the soft mode red-shifts in the frequency because the vibration loses energy to the lattice

https://doi.org/10.1021/acs.chemmater.1c03143
Chem. Mater. XXXX, XXX, XXX−XXX

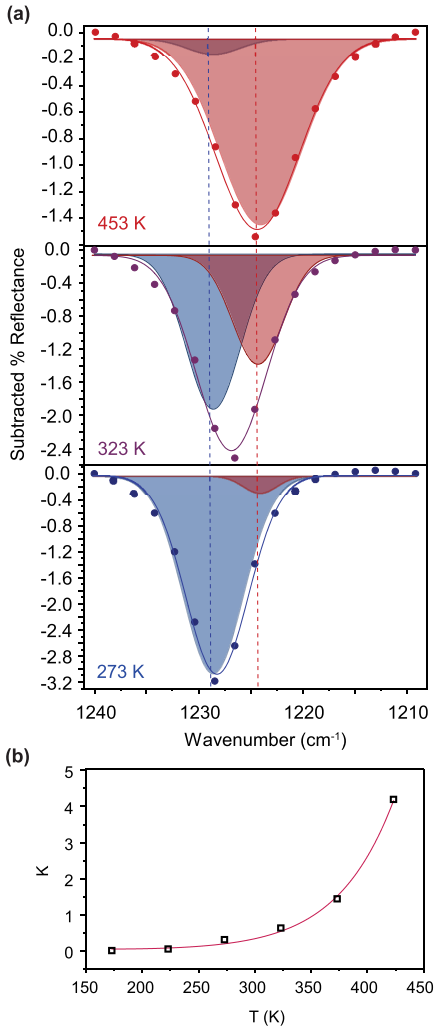

Figure 4. Equilibrium analysis of vibrational mode "X" in $Fe(TA)_2$. Data collected during a cooling cycle. (a) Baseline-subtracted spectra fitted to two species at fixed positions indicated by vertical dashed lines and (b) van't Hoff analysis of equilibrium constants K = [loose]/[tight] versus temperature. The values of [tight] and [loose] were determined from the relative integrated intensities of the high-frequency (blue) and low-frequency (red) species.

undergoing a phase change. Beyond T_c, however, the soft mode blue-shifts toward its new frequency in the new phase.[43,44] Previously, we demonstrated red-shifting carboxylate stretches in carboxylate MOFs and proposed that they arise from metal−carboxylate bond weakening and equilibrium between "tight" and "loose" conformations. Although a blue shift was not observed in these studies, we hypothesized that the critical temperature of a phase change into the "loose" conformation present beyond the decomposition temperature of the MOFs. The data in Figure 3, however, show both an inflection centered at the SCO T_c and the continuation of red shifting at the highest temperatures, therefore exhibiting characteristics of both "tight−loose" and SCO equilibria. During heating, these data indicate red-shifted slopes (χ) of -0.020 cm^{-1} K^{-1}, but upon cooling, the slope increases to -0.035 cm^{-1} K^{-1} in the HS form and then -0.016 cm^{-1} K^{-1} in the LS form. If χ depends on the metal−ligand bonding strength, then the greater slope reflects the expected weaker bonding of HS species. The slight change in the red-shifted slopes in the LS phases before and after the heating cycle may indicate fatigue in the crystalline lattice, as has been observed previously in SCO solids.[45,46]

To investigate whether the temperature-dependent spectra arise from equilibrium phase changes, spectra of vibration X were examined by population analysis, producing excellent fits with a low-temperature higher-frequency species centered at 1228 cm^{-1} (blue) and a high-temperature lower-frequency species centered at 1224 cm^{-1} (red) (Figure 4a). These data derive from a cooling cycle with $Fe(TA)_2$ in the LS state. Akin to prior analysis of carboxylate stretches in MOFs, the positions of both species remain constant across all temperatures, while relative areas change with the high-frequency species giving way to the low-frequency species. Just as weaker metal−carboxylate binding would lead to lower-frequency C−O stretches by increasing the antibonding electron density in the C−O bond vector, weaker metal−triazolate bonding at higher temperatures would produce lower-frequency triazolate stretches. These results strongly suggest that $Fe(TA)_2$ exists in equilibrium between species with strong and weak metal−triazolate bonding, but the microscopic origin remained unclear because both SCO and "loose−tight" transitions could give rise to weaker bonding.

For obtaining thermodynamic insight into the origin of the "strong−weak bonding" equilibrium of $Fe(TA)_2$, van't Hoff analysis was performed on the equilibrium constants K determined from the population fitting of vibration X, where K = [weak]/[strong]. Figure 4b plots K versus temperature for $Fe(TA)_2$ recorded during a cooling cycle just after the HS-to-LS transition. Because [weak] and [strong] are present in equal proportions (K = 1) at around 350 K, these data suggest that "tight−loose" equilibrium contributes to bond weakening at these temperatures. If SCO is the cause, K = 1 would occur at a $T_{cooling}$ of 465 K. The absence of an obvious HS−LS equilibrium at these temperatures is also consistent with the unusually abrupt SCO of $Fe(TA)_2$, which arises from large changes in equilibrium ratios of LS and HS species in a narrow temperature range around $T_{1/2}$. Fitting these data to a modified van't Hoff equation that accounts for changes in the specific heat of the material (ΔC_p), as applied to phase-change materials,[47] produces much larger values than that observed for the "tight−loose" equilibrium of carboxylate MOFs. For LS $Fe(TA)_2$, the fitting gives ΔH = 14.5 kJ mol^{-1}, ΔS = 39.6 J mol^{-1} K, and ΔC_p = 119.7 J mol^{-1} K, whereas analysis of the MOF known as HKUST-1 gave ΔH = 5.9 kJ mol^{-1}, ΔS = 22.0 J mol^{-1} K, and ΔC_p = 37 J mol^{-1} K. The larger ΔH is consistent with the stronger Fe−N bonds of $Fe(TA)_2$, while ΔS and ΔC_p suggest that this process involves greater structural disorder. Although van't Hoff fitting produced higher thermodynamic values versus the carboxylate MOFs, these values are smaller than the SCO parameters ΔH = 33 kJ mol^{-1} and ΔS = 72 J mol^{-1} K previously determined for $Fe(TA)_2$.

To determine whether $Fe(TA)_2$ engages in a "tight−loose" equilibrium in addition to SCO behavior, we investigated the Mn, Co, Cu, and Zn analogues by VT-DRIFTS. Figure 5 shows the spectra of all materials collected between 173 and 623 K. Although $Fe(TA)_2$ displays a single temperature-dependent vibration, the non-SCO analogues exhibit several temperature-dependent bands, which, as calculations suggest, possess a triazolate character (Figures S26−30). Unlike $Fe(TA)_2$, these bands only red-shift at higher temperatures. Although all spectra appear qualitatively similar, we focused our investigation on a single phonon mode in all materials

https://doi.org/10.1021/acs.chemmater.1c03143
Chem. Mater. XXXX, XXX, XXX−XXX

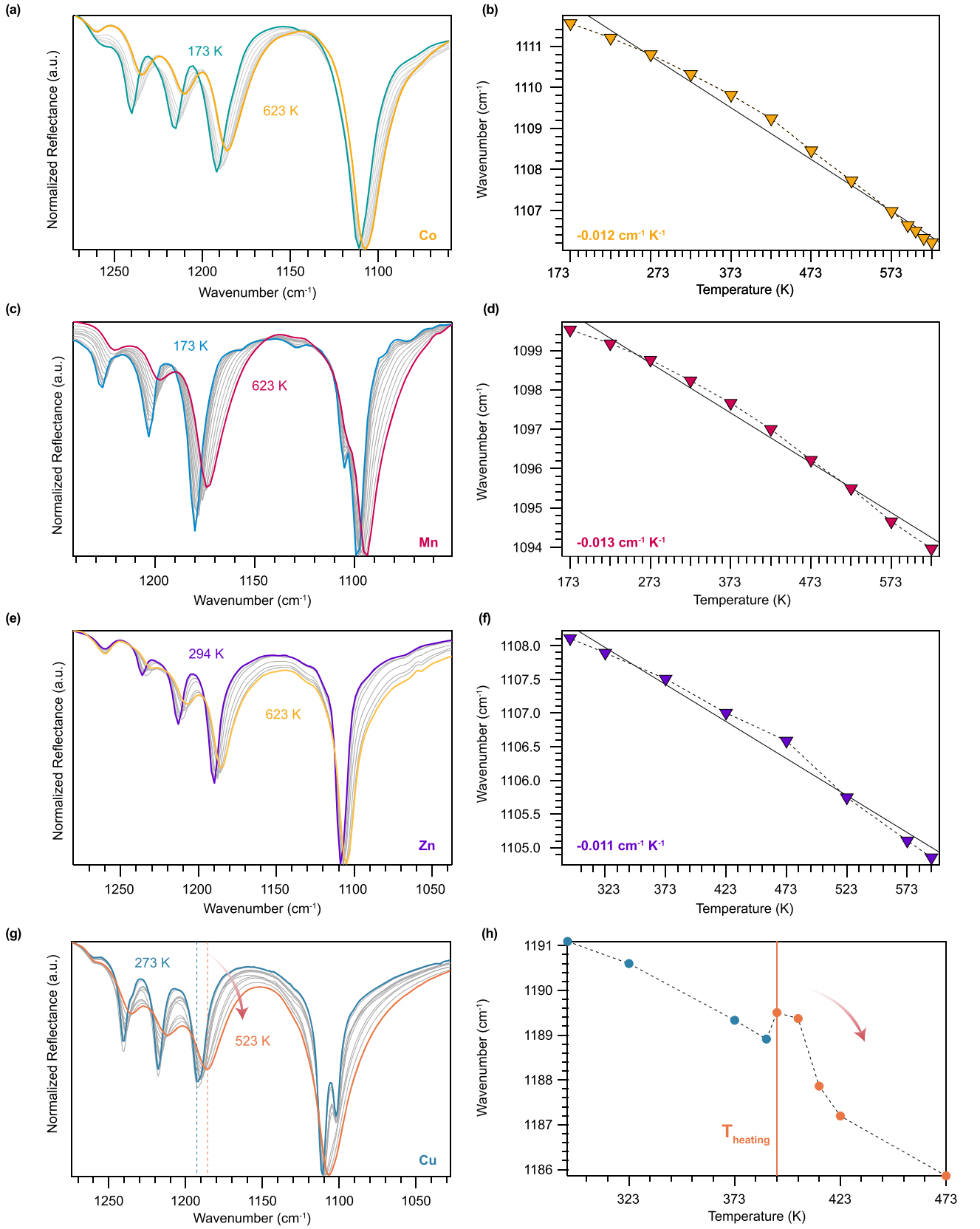

Figure 5. VT-DRIFT spectra of $Co(TA)_2$, $Mn(TA)_2$, $Zn(TA)_2$, and $Cu(TA)_2$ and corresponding peak maxima of vibrational mode "X" in each material. Data were collected during cooling cycles unless indicated otherwise.

around 1180 cm^{-1}, which also appears as the only temperature-dependent mode (vibration X) in $Fe(TA)_2$. As shown in Figure 5b,d,f, the peak maxima of this mode in $Mn(TA)_2$, $Co(TA)_2$, and $Zn(TA)_2$ linearly red-shift at higher temperatures with slopes of around -0.01 cm^{-1} K^{-1}, which are half as steep as those in $Fe(TA)_2$. Shallow slopes could arise from

https://doi.org/10.1021/acs.chemmater.1c03143
Chem. Mater. XXXX, XXX, XXX−XXX

Table 2. Thermal Expansion Coefficients (TEC), Red-Shifted Slopes (χ), Stability Constants ($\ln(K_f)$), and Loose−Tight Thermodynamic Parameters of $M(TA)_2$[a]

MOF	TEC (10^{-6} K^{-1})	slope (cm^{-1} K^{-1})	stability constants	ΔH (kJ mol^{-1})	ΔS (J K^{-1} mol^{-1})	C_p (J K^{-1} mol^{-1})
$Fe(TA)_2$-LS	51.2[a]	−0.020(0)[a] −0.016(0)	1.74			
$Fe(TA)_2$-HS	56.0	−0.035(2)		14.5	39.6	119.7
$Cu(TA)_2$-LT	32.9[a]	−0.023(5)[a]				
−0.014(1)						
$Cu(TA)_2$-HT	1.0[a]	−0.046(0)[a] −0.026(4)	1.97	8.393	17.1	154.7
$Co(TA)_2$	15.2[a]	−0.017(2)	1.09	7.979	16.2	68
$Mn(TA)_2$	20.2[a]	−0.013(1)	0.67	6.841	14.1	80.4
$Zn(TA)_2$	30.6[a]	−0.017(7)	0.91	5.605	24.8	196.1

[a]LS = low-spin state. HS = high-spin state. LT = low-temperature phase. HT = high-temperature phase. [a] obtained from a heating cycle.

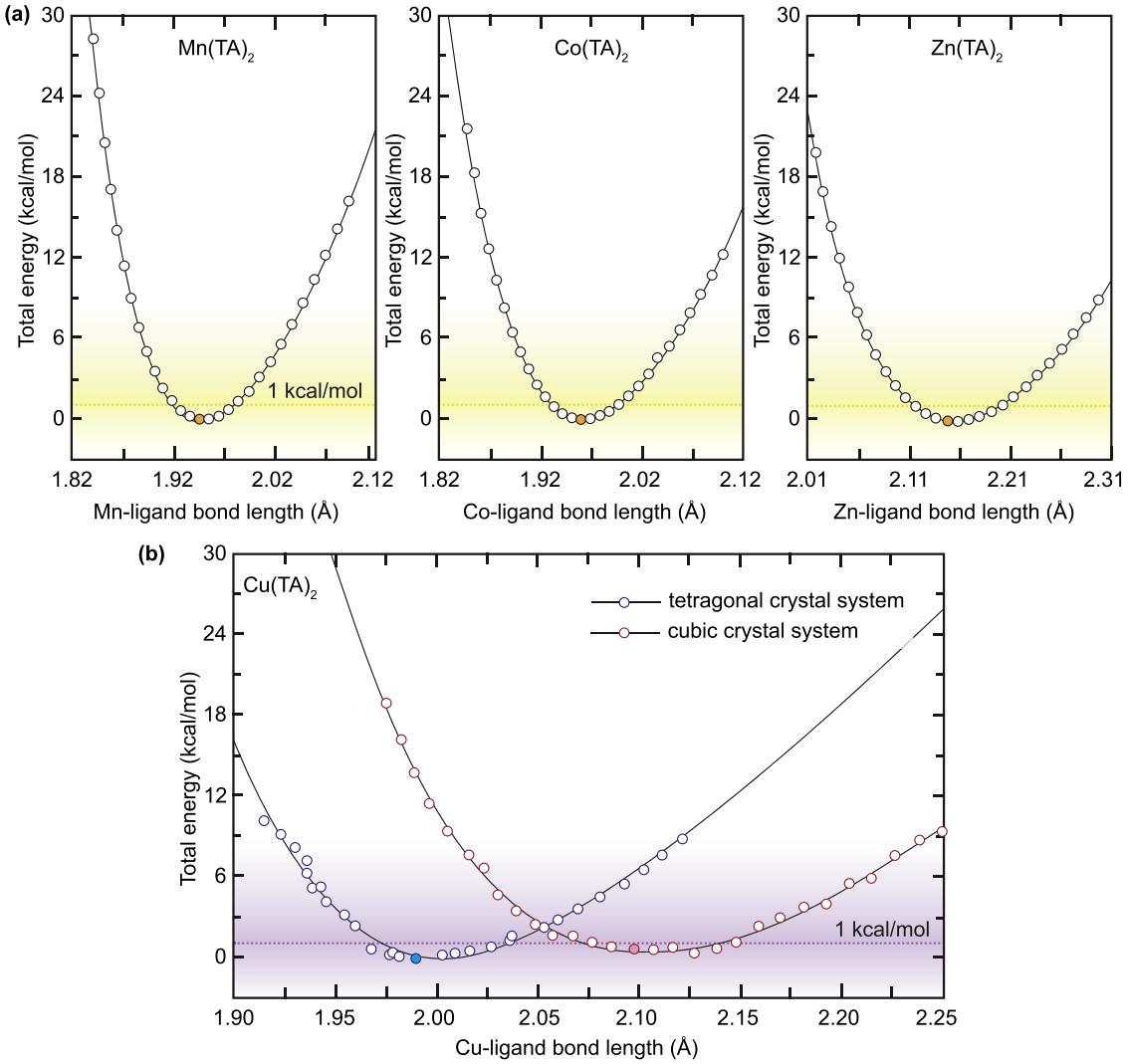

Figure 6. Total energies of geometry-optimized structures versus metal−triazolate bond lengths of (a) $Mn(TA)_2$, $Co(TA)_2$, $Zn(TA)_2$, and (b) $Cu(TA)_2$. Filled circles correspond to ground-state structures.

systems with either less dynamic bonding or from equilibria between species with similar vibrational frequencies, such as ensembles of metal−ligand conformations with degenerate potential energies. Because these slopes are smaller than the χ measured for carboxylate MOFs, we expect that they arise from stronger and less dynamic metal−nitrogen bonding. Unlike the Mn, Co, and Zn analogues, $Cu(TA)_2$ undergoes a phase transition from tetragonal-to-cubic symmetry.[33] Interestingly, the peak maximum of $Cu(TA)_2$ during the warming cycle exhibits a red-shift−blue-shift inflection at the critical temperature (Figure 5h), suggesting that this vibration also serves as a soft mode for $Cu(TA)_2$. Population analysis of this mode in the Mn, Co, Cu, and Zn analogues also supports the presence of two-state equilibria (Figures S6−16), strongly suggesting that $M(TA)_2$ materials undergo a "tight−loose" equilibrium even in the absence of SCO. Interpreting these fits in terms of "tight−loose" ensembles affords conventional 300 K formation constants (K_f = [tight]/[loose]) of all $M(TA)_2$ materials.

https://doi.org/10.1021/acs.chemmater.1c03143
Chem. Mater. XXXX, XXX, XXX−XXX

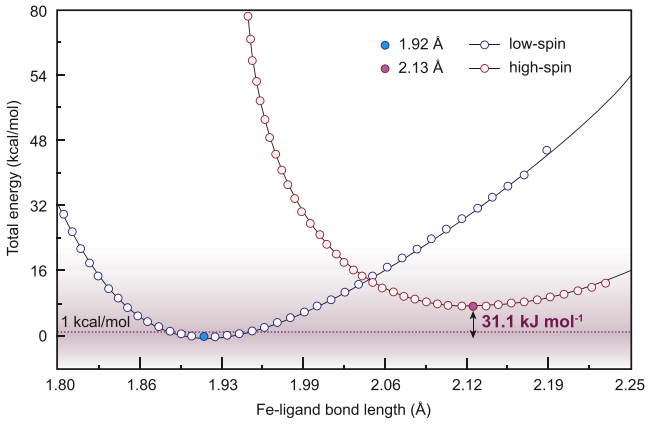

Figure 7. Total energies of geometry-optimized $Fe(TA)_2$ structures versus Fe−triazolate bond lengths. Calculations were performed at 0 K.

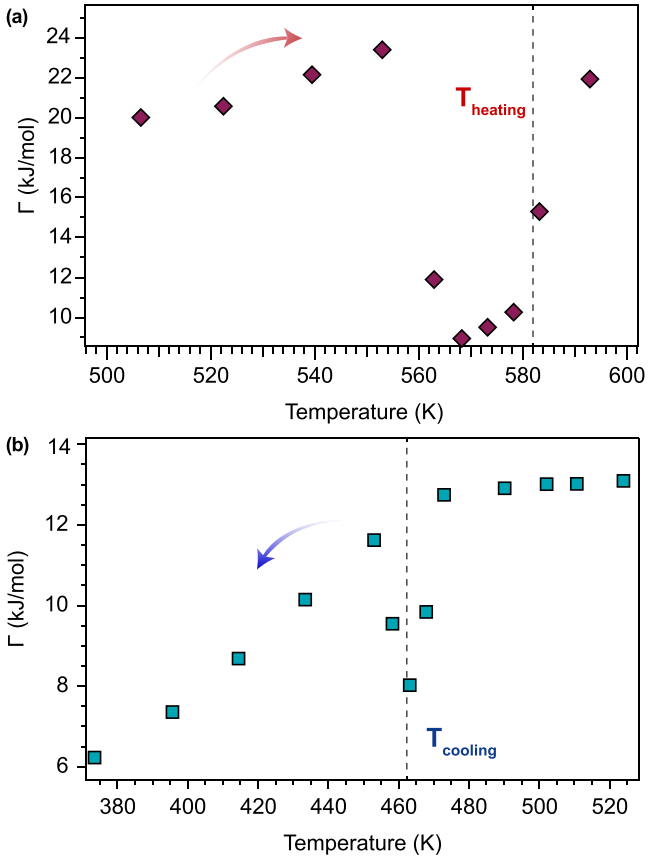

Figure 8. Cooperativity (Γ) determined from eq 1 versus temperature for $Fe(TA)_2$. (a) Cooperativity calculated from the heating cycle magnetic susceptibility data. (b) Cooperativity determined from cooling cycle data.

Comparing $\ln(K_f)$ values, as summarized in Table 2, indicates that the non-phase-change materials (Mn, Co, and Zn) possess the most dynamic bonding. van't Hoff analysis of the Mn, Co, Cu, and Zn analogues (Figures S17−S20) produces ΔH and ΔS comparable to carboxylate MOFs, but with considerably larger ΔC_p (Table 2). Notably, the ΔH and K_f are the smallest for the Mn and Zn analogues, consistent with the labile bonding expected for these ions lacking crystal-field stabilization energies. Comparatively, the ΔH and ΔS values of $Fe(TA)_2$ are approximately twice as large as the other analogues, but they are smaller than the SCO parameters (Table 1), suggesting that they arise from a "tight−loose" rather than SCO equilibrium. Nevertheless, the larger thermodynamic parameters and the presence of only a single soft mode for $Fe(TA)_2$ imply that it proceeds through a markedly different equilibrium process. We propose that vibrations X, Y, and Z red-shift in $M(TA)_2$ materials where only the "tight−loose" equilibrium is relevant, whereas only mode X red-shifts in $Fe(TA)_2$ because it acts as the soft mode driving a separate, competing equilibrium, i.e., the low-spin-to-high-spin phase change. In other words, mode X red-shifts in $Fe(TA)_2$ because it acts as a soft mode to drive SCO, whereas modes X, Y, and Z red-shift in the other materials as a consequence of weakened metal−ligand interactions caused by dynamic bonding.

To further understand the dynamic bonding of $M(TA)_2$ materials, we computed the energies of different metal−ligand conformations. Figure 6 plots the energies of $Mn(TA)_2$, $Co(TA)_2$, $Zn(TA)_2$, and $Cu(TA)_2$ geometries with metal−ligand bond distances that were systematically altered. These "equation of state" diagrams result from uniformly compressing or elongating the entire unit cell volumes and allowing geometries to relax. Energies reflect only enthalpy since the calculations correspond to 0 K. Each data point therefore corresponds to an equilibrium geometry with variable metal−ligand distances. These diagrams are therefore analogous to single-configurational or "reaction" coordinate diagrams. In support of the presence of "tight−loose" equilibria, numerous conformations are accessible through ambient thermal energy, which is indicated by horizontal lines as 1 kcal mol^{-1}. These calculations also reproduce the tetragonal-to-cubic phase change of $Cu(TA)_2$ and demonstrate that both phases possess nearly degenerate conformations that would give rise to "tight−loose" equilibria and red-shifted χ.

Metal−ligand bond distances could be quantified as a function of temperature by experimentally measuring the thermal expansion coefficients (TECs) of all materials. Analysis of high-resolution powder X-ray diffraction patterns (Figures S21−S24) afforded TECs summarized in Table 2. All TECs resemble values determined for conventional carboxylated MOFs showing values of around 10^{-6} K^{-1}, except MOF-5 and HKUST-1, which display negative TECs due to a structural mechanism that likely arises from dynamic bonding.[48−50] The larger TEC parameters for $Fe(TA)_2$ and $Cu(TA)_2$ are consistent with the large volume changes resulting from their phase changes. With experimental TECs, the corresponding metal−ligand conformations could be identified at each temperature. For example, comparing 173 and 623 K geometries, the metal−triazolate bond distances of $Mn(TA)_2$ shift from 1.94 to 1.95 Å, $Co(TA)_2$ from 1.97 to 1.98 Å, $Cu(TA)_2$ from 1.99 to 2.01 Å, and $Zn(TA)_2$ from 2.15 to 2.16 Å. Taken together, these experimental and computational results support the presence of dynamic metal−ligand bonding in the general family of $M(TA)_2$ frameworks.

To understand the relationship between "tight−loose" and SCO behavior in $Fe(TA)_2$, we investigated the energies of iron−triazolate conformations as a function of temperature. Figure 7 plots the energies of LS (blue) and HS (red) $Fe(TA)_2$ conformations with varying iron−nitrogen bond distances. These calculations reproduce the experimental ground-state geometries (filled circles) and the experimentally determined ΔH with high accuracy: the energetic difference between the LS and HS energy curves produces a ΔH of 31.1 kJ mol^{-1}, in

https://doi.org/10.1021/acs.chemmater.1c03143
Chem. Mater. XXXX, XXX, XXX−XXX

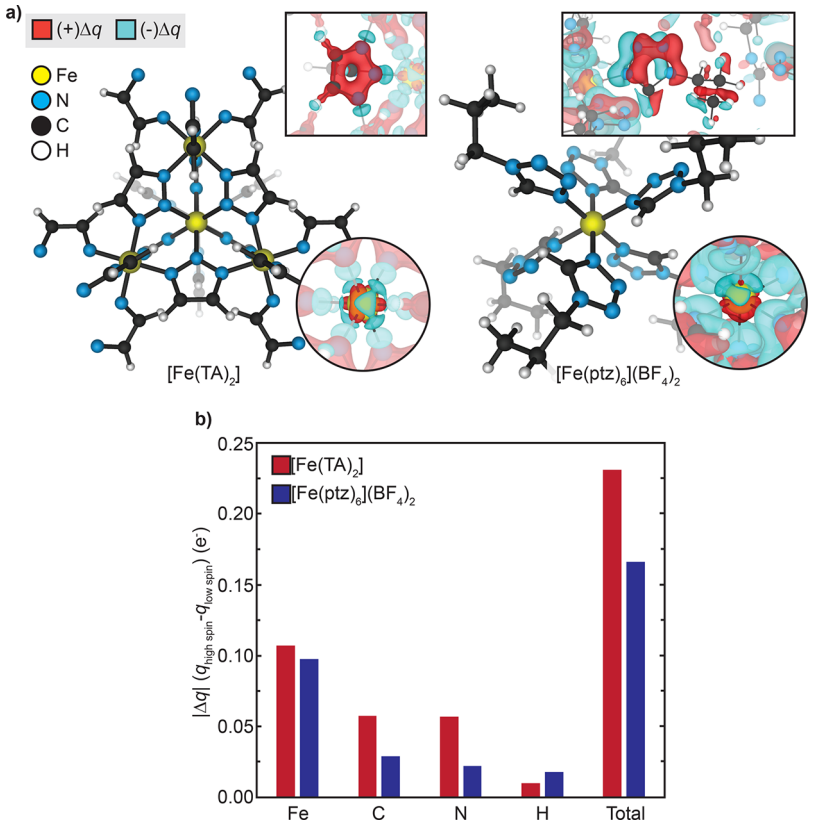

Figure 9. Calculated electron density differences Δq for $Fe(TA)_2$ and $[Fe(ptz)_6][BF_4]_2$ between HS and LS states. (a) Electron density maps. (b) Comparison between absolute differences in electron densities in total and per atom.

excellent agreement with 31.2 kJ mol^{-1} measured by differential scanning calorimetry (Figure S25). The presence of nearly degenerate iron−nitrogen conformations within ambient thermal energy also corroborates the ability of $Fe(TA)_2$ to engage in dynamic bonding. As indicated in Figure 7, the TECs imply that metal−ligand bonds in the LS phase could elongate from 1.91 to 1.93 Å at 583 K prior to SCO. Although the relative energies of the LS and HS curves shift with increased temperature due to entropy, these results suggest that SCO may be enabled by the weakening of iron−nitrogen interactions through dynamic bonding in the LS phase. In other words, vibrational soft modes might serve as the microscopic origin of the unusual SCO cooperativity of $Fe(TA)_2$.

$$\Gamma = \frac{T\left(\Delta S + R \ln \frac{1 - n_{HS}}{n_{HS}}\right) - \Delta H}{1 - 2n_{HS}} \quad (1)$$

For quantitative analysis of cooperativity (Γ) in $Fe(TA)_2$, previously reported magnetic susceptibility data[19] were interpreted in terms of the Slichter−Drickamer model, as outlined in eq 1.[25] Figure 8 plots Γ versus temperature for both cooling and heating cycles by using experimental values for ΔH and ΔS and magnetic susceptibility data to determine n_{HS}, the fraction of HS species at each temperature point. In both cycles, Γ becomes infinite at T_c and levels at large values approximately between 10 and 20 kJ mol^{-1}. A few studies, if any have quantified the value of Γ in SCO frameworks even though they exhibit the largest cooperativity. Most reports on Γ have focused on molecular crystals with weak intermolecular interactions, giving Γ values between 1 and 5 kJ mol^{-1}.[51] A a Γ value of 20 kJ mol^{-1} corresponds to a thermal energy of 2400 K, which is consistent with early predictions[21] that abrupt SCO transitions arise when $\Gamma > k_B T_c$. Given the $T_{heating}$ and $T_{cooling}$ of 582 K and 465, respectively, Γ would correspond to a $k_B T_c$ of roughly 4−5. This analysis, therefore, provides quantitative evidence of the unusually large SCO cooperativity of $Fe(TA)_2$.

With numerical support for large cooperativity and evidence that it relates to vibrational soft modes, we sought deeper microscopic insight into its origin in $Fe(TA)_2$. Previous theoretical reports contended that cooperativity arises from fluctuations in the Madelung field of a SCO material. According to this model, the greater the difference in the electrostatic interactions between the LS and HS states, the greater the energetic driving force (cooperativity) for magnetic centers to drive each other through the spin transition. Quantitatively, the magnitude of cooperativity depends directly on the difference in the metal−ligand bond polarizations $\Delta\delta V$ and the electron density distributions Δq of the LS versus HS states,[52] i.e., $\Gamma = \Delta q \times \Delta\delta V$. To explore the ability of this model to account for the large Γ in $Fe(TA)_2$, we calculated Δq for both $Fe(TA)_2$ and a related molecular crystal of $[Fe(ptz)_6](BF_4)_2$ (ptz = 1-propyltetrazolate). Figure 9a shows the increased (red) and decreased (blue) Δq of both systems in the HS state relative to the LS states. In both systems, electron density shifts away from the metal−ligand bonding orbitals toward the ligand accepting orbitals. Additionally, inspection of the metal centers indicates rearrangement of electron density within the d-orbitals, as expected for a spin transition. For quantitative comparison of Δq, Figure 9b plots $|\Delta q|$ as a histogram. Although $Fe(TA)_2$ shows slightly higher changes in the electron density on the Fe centers, it

https://doi.org/10.1021/acs.chemmater.1c03143
Chem. Mater. XXXX, XXX, XXX−XXX

exhibits a far larger change on the ligands to produce a total $|\Delta q|$ nearly 50% greater per formula unit compared to the molecular analogue. Considered together, these results, therefore, suggest that the large cooperativity of $Fe(TA)_2$, and perhaps frameworks in general, derives from vibrational soft modes that induce large differences in electron density along the metal−ligand unit. Compared to other molecular and solid-state SCO materials, we propose that MOFs occupy a perfect middle-ground state between the weak intermolecular interactions of molecular crystals and the strong covalent bonding of conventional semiconductors. Due to ionic metal−linker interactions that engage in dynamic bonding with high polarizability, cooperativity is especially strong, leading to a unique SCO behavior. The importance of dynamic bonding in driving SCO might also explain the strong size dependence of SCO particles, where large domain sizes exhibit larger hysteresis windows at higher temperatures and more abrupt transitions.[53−58] Specifically, we expect greater bond dynamics in smaller particles due to their more flexible structures, thereby permitting SCO with less thermal energy compared to large domain sizes.

CONCLUSIONS

In conclusion, VT-DRIFTS provides evidence for both dynamic metal−linker bonding in the family of $M(TA)_2$ MOFs and hallmark signatures of soft modes at the SCO temperature of $Fe(TA)_2$. These results suggest that the unusual SCO cooperativity of $Fe(TA)_2$ derives from the particularly dynamic vibrations of MOFs, in general. Modeling magnetic susceptibility data allows quantification of cooperativity, affording energetic values several orders of magnitude larger than that reported for nonframework systems. To identify the origin of this large cooperativity, computational analysis of electron density in the HS and LS $Fe(TA)_2$ structures was performed, revealing a much larger difference across metal−linker bonds compared to molecular analogues. As predicted by previous theoretical studies, such considerable changes in bond polarization, as induced by collective vibrations, trigger fluctuations in the Madelung fields thereby electrostatically stabilizing spin transitions. These results, therefore, provide a microscopic mechanism and quantitative analysis of SCO cooperativity for outlining the general design of materials with cooperative magnetism.

ASSOCIATED CONTENT

Supporting Information

The Supporting Information is available free of charge at https://pubs.acs.org/doi/10.1021/acs.chemmater.1c03143.

Experimental methods with materials and characterization details; MOF syntheses; VT-DRIFTS of $Fe(TA)_2$ (S1), $Cu(TA)_2$ (S2), $Mn(TA)_2$ (S3), $Co(TA)_2$ (S4), and $Zn(TA)_2$ (S5); equilibrium model and fitting description; population plots of $Fe(TA)_2$ (S6), subtracted reflectance and population plots of $Cu(TA)_2$ (S7−S10), $Mn(TA)_2$ (S11 and S12), $Co(TA)_2$ (S13 and S14), and $Zn(TA)_2$ (S15 and S16); van't Hoff analysis from the cooling cycle data of $Cu(TA)_2$ (S17), $Mn(TA)_2$ (S18), $Co(TA)_2$ (S19), and $Zn(TA)_2$ (S20); tabulated cell parameters (Table S1) and VT-PXRD data of $Mn(TA)_2$ during the heating cycle (S21), $Fe(TA)_2$ during the heating cycle followed by cooling (S22), $Co(TA)_2$ during the heating cycle (S23), and $Cu(TA)_2$ during the heating cycle (S24); DSC data of $Fe(TA)_2$ (S25); computational methods and simulated vibrational spectra overlayed with VT-DRIFT spectra transformed with the Kubelka−Munk function followed by tabulated frequencies of expected vibrational modes in $Fe(TA)_2$ (S26, Table S2), $Cu(TA)_2$ (S27, Table S3), $Mn(TA)_2$ (S28, Table S4), $Co(TA)_2$ (S29, Table S5), and $Zn(TA)_2$ (S30, Table S6) (PDF)

AUTHOR INFORMATION

Corresponding Authors

Christopher H. Hendon − *Department of Chemistry and Biochemistry, Material Science Institute, University of Oregon, Eugene, Oregon 97403, United States;* orcid.org/0000-0002-7132-768X; Email: chendon@uoregon.edu

Carl K. Brozek − *Department of Chemistry and Biochemistry, Material Science Institute, University of Oregon, Eugene, Oregon 97403, United States;* orcid.org/0000-0002-8014-7904; Email: cbrozek@uoregon.edu

Authors

Anastasia B. Andreeva − *Department of Chemistry and Biochemistry, Material Science Institute, University of Oregon, Eugene, Oregon 97403, United States*

Khoa N. Le − *Department of Chemistry and Biochemistry, Material Science Institute, University of Oregon, Eugene, Oregon 97403, United States*

Kentaro Kadota − *Department of Chemistry and Biochemistry, Material Science Institute, University of Oregon, Eugene, Oregon 97403, United States*

Satoshi Horike − *Department of Synthetic Chemistry and Biological Chemistry, Graduate School of Engineering, Kyoto University, Kyoto 615-8510, Japan;* orcid.org/0000-0001-8530-6364

Complete contact information is available at: https://pubs.acs.org/10.1021/acs.chemmater.1c03143

Notes

The authors declare no competing financial interest.

ACKNOWLEDGMENTS

The authors gratefully acknowledge the University of Oregon for startup funds. This work made use of the CAMCOR facility of the Lorry I. Lokey Laboratories at the University of Oregon to perform the VT-DRIFTS experiments. This material is based on the work supported by the National Science Foundation through the Division of Materials Research under grant no. DMR-1956403, by the Department of Energy through the Office of Basic Energy Sciences under grant no. DE-SC0022147, and by the University of Oregon under Mini Grant and Presidential Undergraduate Research Scholars program through the Office of Vice President for Research and Innovation.

REFERENCES

(1) Nicolazzi, W.; Bousseksou, A. Thermodynamical Aspects of the Spin Crossover Phenomenon. *C. R. Chim.* **2018**, *21*, 1060−1074.

(2) Takahashi, K. Spin-Crossover Complexes. *Inorganics* **2018**, *6*, No. 32.

(3) Kitazawa, T. Synthesis and Applications of New Spin Crossover Compounds. *Crystals* **2019**, *9*, No. 382.

(4) Gütlich, P.; Hauser, A.; Spiering, H. Thermal and Optical Switching of Iron(II) Complexes. *Angew. Chem., Int. Ed.* **1994**, *33*, 2024−2054.
(5) Gütlich, P.; Goodwin, A. *Spin Crossover in Transition Metal Compounds*; Springer: Heidelberg, 2004.
(6) Halcrow, M. A. Spin-Crossover. In *Materials − Properties and Applications*; John Wiley & Sons, Inc.: Chichester, UK, 2013.
(7) Chorazy, S.; Charytanowicz, T.; Pinkowicz, D.; Wang, J.; Nakabayashi, K.; Klimke, S.; Renz, F.; Ohkoshi, S.; Sieklucka, B. Octacyanidorhenate(V) Ion as an Efficient Linker for Hysteretic Two-Step Iron(II) Spin Crossover Switchable by Temperature, Light, and Pressure. *Angew. Chem., Int. Ed.* **2020**, *59*, 15741−15749.
(8) Kahn, O. Spin-Crossover Molecular Materials. *Curr. Opin. Solid State Mater. Sci.* **1996**, *1*, 547−554.
(9) Valverde-Muñoz, F. J.; Kazan, R.; Boukheddaden, K.; Ohba, M.; Real, J. A.; Delgado, T. Downsizing of Nanocrystals While Retaining Bistable Spin Crossover Properties in Three-Dimensional Hofmann-Type {Fe(Pz)[Pt(CN)$_4$]}−Iodine Adducts. *Inorg. Chem.* **2021**, *60*, 8851−8860.
(10) Ohtani, R.; Yoneda, K.; Furukawa, S.; Horike, N.; Kitagawa, S.; Gaspar, A. B.; Muñoz, M. C.; Real, J. A.; Ohba, M. Precise Control and Consecutive Modulation of Spin Transition Temperature Using Chemical Migration in Porous Coordination Polymers. *J. Am. Chem. Soc.* **2011**, *133*, 8600−8605.
(11) Kitazawa, T.; Gomi, Y.; Takahashi, M.; Takeda, M.; Enomoto, M.; Miyazaki, A.; Enoki, T. Spin-Crossover Behaviour of the Coordination Polymer $Fe^{II}(C_5H_5N)_2Ni^{II}(CN)_4$. *J. Mater. Chem.* **1996**, *6*, 119−121.
(12) Southon, P. D.; Liu, L.; Fellows, E. A.; Price, D. J.; Halder, G. J.; Chapman, K. W.; Moubaraki, B.; Murray, K. S.; Létard, J. F.; Kepert, C. J. Dynamic Interplay between Spin-Crossover and Host-Guest Function in a Nanoporous Metal-Organic Framework Material. *J. Am. Chem. Soc.* **2009**, *131*, 10998−11009.
(13) Sciortino, N. F.; Scherl-Gruenwald, K. R.; Chastanet, G.; Halder, G. J.; Chapman, K. W.; Létard, J.-F.; Kepert, C. J. Hysteretic Three-Step Spin Crossover in a Thermo- and Photochromic 3D Pillared Hofmann-Type Metal−Organic Framework. *Angew. Chem., Int. Ed.* **2012**, *51*, 10154−10158.
(14) Zenere, K. A.; Duyker, S. G.; Trzop, E.; Collet, E.; Chan, B.; Doheny, P. W.; Kepert, C. J.; Neville, S. M. Increasing Spin Crossover Cooperativity in 2D Hofmann-Type Materials with Guest Molecule Removal. *Chem. Sci.* **2018**, *9*, 5623−5629.
(15) Sciortino, N. F.; Neville, S. M.; Létard, J.-F.; Moubaraki, B.; Murray, K. S.; Kepert, C. J. Thermal- and Light-Induced Spin-Crossover Bistability in a Disrupted Hofmann-Type 3D Framework. *Inorg. Chem.* **2014**, *53*, 7886−7893.
(16) Kosaka, W.; Nomura, K.; Hashimoto, K.; Ohkoshi, S. I. Observation of an Fe(II) Spin-Crossover in a Cesium Iron Hexacyanochromate. *J. Am. Chem. Soc.* **2005**, *127*, 8590−8591.
(17) Boström, H. L. B.; Cairns, A. B.; Liu, L.; Lazor, P.; Collings, I. E. Spin Crossover in the Prussian Blue Analogue $FePt(CN)_6$ Induced by Pressure or X-Ray Irradiation. *Dalton Trans.* **2020**, *49*, 12940−12944.
(18) Rodríguez-Velamazán, J. A.; González, M. A.; Real, J. A.; Castro, M.; Muñoz, M. C.; Gaspar, A. B.; Ohtani, R.; Ohba, M.; Yoneda, K.; Hijikata, Y.; Yanai, N.; Mizuno, M.; Ando, H.; Kitagawa, S. A Switchable Molecular Rotator: Neutron Spectroscopy Study on a Polymeric Spin-Crossover Compound. *J. Am. Chem. Soc.* **2012**, *134*, 5083−5089.
(19) Grzywa, M.; Röß-Ohlenroth, R.; Muschielok, C.; Oberhofer, H.; Błachowski, A.; Żukrowski, J.; Vieweg, D.; Von Nidda, H. A. K.; Volkmer, D. Cooperative Large-Hysteresis Spin-Crossover Transition in the Iron(II) Triazolate [Fe(TA)$_2$] Metal-Organic Framework. *Inorg. Chem.* **2020**, *59*, 10501−10511.
(20) Ohnishi, S.; Sugano, S. Strain Interaction Effects on the High-Spin-Low-Spin Transition of Transition-Metal Compounds. *J. Phys. C: Solid State Phys.* **1981**, *14*, 39−55.
(21) Zimmermann, R.; König, E. A Model for High-Spin/Low-Spin Transitions in Solids Including the Effect of Lattice Vibrations. *J. Phys. Chem. Solids* **1977**, *38*, 779−788.
(22) Kambara, T. Theory of High-spin⇄low-spin Transitions in Transition Metal Compounds Induced by Cooperative Molecular Distortions and Lattice Strains. *J. Chem. Phys.* **1981**, *74*, 4557−4565.
(23) Sasaki, N.; Kambara, T. The Effect of a Magnetic Field on the High Spin to or from Low-Spin Transitions in Ferrous and Ferric Compounds. *J. Phys. C: Solid State Phys.* **1982**, *15*, 1035−1071.
(24) Hauser, A.; Gutlich, P.; Spiering, H. High-Spin → Low-Spin Relaxation Kinetics and Cooperative Effects in the $[Fe(Ptz)_6](BF_4)_2$ and $[Zn_{1-x}Fe_x(Ptz)_6](BF_4)_2$ (Ptz = 1-Propyltetrazole) Spin-Crossover Systems. *Inorg. Chem.* **1986**, *25*, 4245−4248.
(25) Slichter, C. P.; Drickamer, H. G. Pressure-Induced Electronic Changes in Compounds of Iron. *J. Chem. Phys.* **1972**, *56*, 2142−2160.
(26) Sorai, M.; Seki, S. Phonon Coupled Cooperative Low-Spin $^1A_1$ High-Spin $^5T_2$ Transition in $[Fe(Phen)_2(NCS)_2]$ and $[Fe(Phen)_2(NCSe)_2]$ Crystals. *J. Phys. Chem. Solids* **1974**, *35*, 555−570.
(27) Willenbacher, N.; Spiering, H. The Elastic Interaction of High-Spin and Low-Spin Complex Molecules in Spin-Crossover Compounds. *J. Phys. C: Solid State Phys.* **1988**, *21*, 1423−1439.
(28) Andreeva, A. B.; Le, K. N.; Chen, L.; Kellman, M. E.; Hendon, C. H.; Brozek, C. K. Soft Mode Metal-Linker Dynamics in Carboxylate MOFs Evidenced by Variable-Temperature Infrared Spectroscopy. *J. Am. Chem. Soc.* **2020**, *142*, 19291−19299.
(29) Fabrizio, K.; Lazarou, K. A.; Payne, L. I.; Twight, L. P.; Golledge, S.; Hendon, C. H.; Brozek, C. K. Tunable Band Gaps in MUV-10(M): A Family of Photoredox-Active MOFs with Earth-Abundant Open Metal Sites. *J. Am. Chem. Soc.* **2021**, *143*, 12609−12621.
(30) Altomare, A.; Cuocci, C.; Giacovazzo, C.; Moliterni, A.; Rizzi, R.; Corriero, N.; Falcicchio, A. EXPO2013: A Kit of Tools for Phasing Crystal Structures from Powder Data. *J. Appl. Crystallogr.* **2013**, *46*, 1231−1235.
(31) Kresse, G.; Furthmüller, J. Efficiency of Ab-Initio Total Energy Calculations for Metals and Semiconductors Using a Plane-Wave Basis Set. *Comput. Mater. Sci.* **1996**, *6*, 15−50.
(32) Perdew, J. P.; Burke, K.; Ernzerhof, M. Generalized Gradient Approximation Made Simple. *Phys. Rev. Lett.* **1996**, *77*, 3865.
(33) Grzywa, M.; Denysenko, D.; Hanss, J.; Scheidt, E. W.; Scherer, W.; Weil, M.; Volkmer, D. CuN_6 Jahn-Teller Centers in Coordination Frameworks Comprising Fully Condensed Kuratowski-Type Secondary Building Units: Phase Transitions and Magneto-Structural Correlations. *Dalton Trans.* **2012**, *41*, 4239−4248.
(34) Krukau, A. V.; Vydrov, O. A.; Izmaylov, A. F.; Scuseria, G. E. Influence of the Exchange Screening Parameter on the Performance of Screened Hybrid Functionals. *J. Chem. Phys.* **2006**, *125*, No. 224106.
(35) Kroeber, J.; Audiere, J.-P.; Claude, R.; Codjovi, E.; Kahn, O.; Haasnoot, J. G.; Groliere, F.; Jay, C.; Bousseksou, A. Spin Transitions and Thermal Hysteresis in the Molecular-Based Materials [Fe(Htrz)$_2$(Trz)](BF$_4$) and $[Fe(Htrz)_3](BF_4)_2 \bullet H_2O$ (Htrz = 1,2,4-4H-Triazole; Trz = 1,2,4-Triazolato). *Chem. Mater.* **1994**, *6*, 1404−1412.
(36) Hosoya, K.; Kitazawa, T.; Takahashi, M.; Takeda, M.; Meunier, J.-F.; Molnár, G.; Bousseksou, A. Unexpected Isotope Effect on the Spin Transition of the Coordination Polymer $Fe(C_5H_5N)_2[Ni(CN)_4]$. *Phys. Chem. Chem. Phys.* **2003**, *5*, 1682−1688.
(37) Liu, W.; Wang, L.; Su, Y.-J.; Chen, Y.-C.; Tucek, J.; Zboril, R.; Ni, Z.-P.; Tong, M.-L. Hysteretic Spin Crossover in Two-Dimensional (2D) Hofmann-Type Coordination Polymers. *Inorg. Chem.* **2015**, *54*, 8711−8716.
(38) Niel, V.; Martinez-Agudo, J. M.; Muñoz, M. C.; Gaspar, A. B.; Real, J. A. Cooperative Spin Crossover Behavior in Cyanide-Bridged Fe(II)−M(II) Bimetallic 3D Hofmann-like Networks (M = Ni, Pd, and Pt). *Inorg. Chem.* **2001**, *40*, 3838−3839.
(39) Mullaney, B. R.; Goux-Capes, L.; Price, D. J.; Chastanet, G.; Létard, J. F.; Kepert, C. J. Spin Crossover-Induced Colossal Positive and Negative Thermal Expansion in a Nanoporous Coordination Framework Material. *Nat. Commun.* **2017**, *8*, No. 1053.

https://doi.org/10.1021/acs.chemmater.1c03143
Chem. Mater. XXXX, XXX, XXX−XXX

(40) Scepaniak, J. J.; Harris, T. D.; Vogel, C. S.; Sutter, J.; Meyer, K.; Smith, J. M. Spin Crossover in a Four-Coordinate Iron(II) Complex. *J. Am. Chem. Soc.* **2011**, *133*, 3824−3827.
(41) Capes, L.; Létard, J.-F.; Kahn, O. Photomagnetic Properties in a Series of Spin Crossover Compounds $[Fe(PM\text{-}L)_2(NCX)_2]$ (X=S, Se) with Substituted 2′-Pyridylmethylene- 4-Amino Ligands. *Chem. - Eur. J.* **2000**, *6*, 2246−2255.
(42) Gándara, F.; Uribe-Romo, F. J.; Britt, D. K.; Furukawa, H.; Lei, L.; Cheng, R.; Duan, X.; O'Keeffe, M.; Yaghi, O. M. Porous, Conductive Metal-Triazolates and Their Structural Elucidation by the Charge-Flipping Method. *Chem. - Eur. J.* **2012**, *18*, 10595−10601.
(43) Venkataraman, G. Soft Modes and Structural Phase Transitions. *Bull. Mater. Sci.* **1979**, *1*, 129−170.
(44) Scott, J. F. Soft-Mode Spectroscopy: Experimental Studies of Structural Phase Transitions. *Rev. Mod. Phys.* **1974**, *46*, 83−128.
(45) Sanchis-Gual, R.; Torres-Cavanillas, R.; Coronado-Puchau, M.; Giménez-Marqués, M.; Coronado, E. Plasmon-Assisted Spin Transition in Gold Nanostar@spin Crossover Heterostructures. *J. Mater. Chem. C* **2021**, *9*, 10811−10818.
(46) Brooker, S. Spin Crossover with Thermal Hysteresis: Practicalities and Lessons Learnt. *Chem. Soc. Rev.* **2015**, *44*, 2880−2892.
(47) Huang, C. Y.; Wang, T.; Gai, F. Temperature Dependence of the CN Stretching Vibration of a Nitrile-Derivatized Phenylalanine in Water. *Chem. Phys. Lett.* **2003**, *371*, 731−738.
(48) Lock, N.; Wu, Y.; Christensen, M.; Cameron, L. J.; Peterson, V. K.; Bridgeman, A. J.; Kepert, C. J.; Iversen, B. B. Elucidating Negative Thermal Expansion in MOF-5. *J. Phys. Chem. C* **2010**, *114*, 16181−16186.
(49) Wu, Y.; Kobayashi, A.; Halder, G. J.; Peterson, V. K.; Chapman, K. W.; Lock, N.; Southon, P. D.; Kepert, C. J. Negative Thermal Expansion in the Metal-Organic Framework Material Cu 3(1,3,5-Benzenetricarboxylate)2. *Angew. Chem., Int. Ed.* **2008**, *47*, 8929−8932.
(50) Zhou, W.; Wu, H.; Yildirim, T.; Simpson, J. R.; Walker, A. R. H. Origin of the Exceptional Negative Thermal Expansion in Metal-Organic Framework-5 Zn_4O (1,4-Benzenedicarboxylate)$_3$. *Phys. Rev. B* **2008**, *78*, No. 054114.
(51) Shen, F. X.; Pi, Q.; Shi, L.; Shao, D.; Li, H. Q.; Sun, Y. C.; Wang, X. Y. Spin Crossover in Hydrogen-Bonded Frameworks of Fe^{II} Complexes with Organodisulfonate Anions. *Dalton Trans.* **2019**, *48*, 8815−8825.
(52) Kepenekian, M.; Le Guennic, B.; Robert, V. Magnetic Bistability: From Microscopic to Macroscopic Understandings of Hysteretic Behavior Using Ab Initio Calculations. *Phys. Rev. B* **2009**, *79*, No. 094428.
(53) Torres-Cavanillas, R.; Sanchis-Gual, R.; Dugay, J.; Coronado-Puchau, M.; Giménez-Marqués, M.; Coronado, E. Design of Bistable Gold@Spin-Crossover Core−Shell Nanoparticles Showing Large Electrical Responses for the Spin Switching. *Adv. Mater.* **2019**, *31*, No. 1900039.
(54) Forestier, T.; Kaiba, A.; Pechev, S.; Denux, D.; Guionneau, P.; Etrillard, C.; Daro, N.; Freysz, E.; Létard, J.-F. Nanoparticles of $[Fe(NH_2\text{-}Trz)_3]Br_2{\cdot}3H_2O$ (NH_2-Trz = 2-Amino-1,2,4-Triazole) Prepared by the Reverse Micelle Technique: Influence of Particle and Coherent Domain Sizes on Spin-Crossover Properties. *Chem. - Eur. J.* **2009**, *15*, 6122−6130.
(55) Boldog, I.; Gaspar, A. B.; Martínez, V.; Pardo-Ibañez, P.; Ksenofontov, V.; Bhattacharjee, A.; Gütlich, P.; Real, J. A. Spin-Crossover Nanocrystals with Magnetic, Optical, and Structural Bistability Near Room Temperature. *Angew. Chem., Int. Ed.* **2008**, *47*, 6433−6437.
(56) Larionova, J.; Salmon, L.; Guari, Y.; Tokarev, A.; Molvinger, K.; Molnár, G.; Bousseksou, A. Towards the Ultimate Size Limit of the Memory Effect in Spin-Crossover Solids. *Angew. Chem., Int. Ed.* **2008**, *47*, 8236−8240.
(57) Coronado, E.; Galán-Mascarós, J. R.; Monrabal-Capilla, M.; García-Martínez, J.; Pardo-Ibáñez, P. Bistable Spin-Crossover Nanoparticles Showing Magnetic Thermal Hysteresis near Room Temperature. *Adv. Mater.* **2007**, *19*, 1359−1361.
(58) Volatron, F.; Catala, L.; Rivière, E.; Gloter, A.; Stéphan, O.; Mallah, T. Spin-Crossover Coordination Nanoparticles. *Inorg. Chem.* **2008**, *47*, 6584−6586.

https://doi.org/10.1021/acs.chemmater.1c03143
Chem. Mater. XXXX, XXX, XXX−XXX